Technology

Developmental Cell

Quantitative Multiscale Cell Imaging in Controlled 3D Microenvironments

Highlights

- meSPIM allows microenvironmentally conscious 3D imaging/analysis of subcellular biology
- Precisely controlled microenvironments reveal diverse morphological phenotypes
- Isotropic resolution and high speed enable the quantification of 3D cell signaling and morphodynamics
- Multiscale quantification of microenvironmental reorganization by cells

Authors

Erik S. Welf, Meghan K. Driscoll, Kevin M. Dean, ..., Michael Z. Lin, Gaudenz Danuser, Reto Fiolka

Correspondence

gaudenz.danuser@utsouthwestern.edu (G.D.), reto.fiolka@utsouthwestern.edu (R.F.)

In Brief

Cell microenvironment critically regulates function, but microscopy limitations have hindered the study of realistic cellular behavior in vitro. Welf, Driscoll et al. developed meSPIM, a microscope and analytical framework facilitating quantitative 3D analysis of intracellular signaling and submicrometer cellular structures along with large-scale cell morphological/environmental features in more realistic microenvironments.

Welf et al., 2016, Developmental Cell *36*, 462–475
February 22, 2016
http://dx.doi.org/10.1016/j.devcel.2016.01.022

CellPress

CellPress

Developmental Cell
Technology

Quantitative Multiscale Cell Imaging in Controlled 3D Microenvironments

Erik S. Welf,[1,4] Meghan K. Driscoll,[1,4] Kevin M. Dean,[1] Claudia Schäfer,[1] Jun Chu,[2] Michael W. Davidson,[3] Michael Z. Lin,[2] Gaudenz Danuser,[1,*] and Reto Fiolka[1,*]
[1]Department of Cell Biology, University of Texas Southwestern Medical Center, Dallas, TX 75390, USA
[2]Departments of Bioengineering and Pediatrics, Stanford University, Stanford, CA 94305, USA
[3]National High Magnetic Field Laboratory, Department of Biological Science, Florida State University, Tallahassee, FL 32310, USA
[4]Co-first author
*Correspondence: gaudenz.danuser@utsouthwestern.edu (G.D.), reto.fiolka@utsouthwestern.edu (R.F.)
http://dx.doi.org/10.1016/j.devcel.2016.01.022

SUMMARY

The microenvironment determines cell behavior, but the underlying molecular mechanisms are poorly understood because quantitative studies of cell signaling and behavior have been challenging due to insufficient spatial and/or temporal resolution and limitations on microenvironmental control. Here we introduce microenvironmental selective plane illumination microscopy (meSPIM) for imaging and quantification of intracellular signaling and submicrometer cellular structures as well as large-scale cell morphological and environmental features. We demonstrate the utility of this approach by showing that the mechanical properties of the microenvironment regulate the transition of melanoma cells from actin-driven protrusion to blebbing, and we present tools to quantify how cells manipulate individual collagen fibers. We leverage the nearly isotropic resolution of meSPIM to quantify the local concentration of actin and phosphatidylinositol 3-kinase signaling on the surfaces of cells deep within 3D collagen matrices and track the many small membrane protrusions that appear in these more physiologically relevant environments.

INTRODUCTION

Cells in vivo function in complex three-dimensional (3D) microenvironments consisting of cells and extracellular matrix (ECM). In addition to the well-known pathways governed by the biochemical properties of the ECM, a wide range of cell behaviors including cancer cell invasion and progenitor cell differentiation are controlled by the mechanical properties of the cellular microenvironment (Discher et al., 2009; Pickup et al., 2014). Although recent work has shown that the microenvironmental properties of the stroma mediate critical functions, such as drug resistance in cancer cells (Hirata et al., 2015), we have very little understanding of how a cell's microenvironment influences the spatial and temporal organization of molecular signaling pathways. The quantitative approaches necessary to extract such spatiotemporal information have provided valuable insight into how protein spatial distribution and activity regulate cell behaviors (Lee et al., 2015; Plotnikov et al., 2012; Spiller et al., 2010; Welf and Danuser, 2014). Unfortunately, the ability to quantify cell signaling and morphological changes in 3D environments demands specific temporal and spatial resolution in imaging (Vilela et al., 2013) that is not achievable by existing microscopy approaches. As a result, the ability to quantify cell signaling and morphology has so far been limited to very restrictive conditions.

Quantification of cell signaling and morphology in 3D microenvironments requires imaging that meets specific performance criteria. First, the microscope design must not prohibitively constrain microenvironmental properties. Specifically, researchers must be able to tune the sample environment without unavoidable chemical or mechanical influences such as the presence of a glass coverslip. Second, spatial and temporal resolution must match the cellular features of interest. For many cellular processes, this requires submicrometer spatial resolution to capture small features, but also requires a large field of view to capture the overall cell phenotype and microenvironmental structures. This also requires fast temporal sampling in order to capture the dynamics of cell signaling events occurring at timescales on the order of seconds. Third, spatial resolution must be isotropic to avoid spatial bias in quantitative measurements. Thus, axial resolution that is comparable with the lateral resolving power is critical. In 3D cell movements, signaling and the structures composing the extracellular environment extend in all directions without lateral confinement or bias. Nearly isotropic resolution also greatly simplifies quantitative image analysis, by allowing methods to be adapted from 2D image analysis rather than having to be reinvented to contend with anisotropic resolution. We know of no existing imaging modalities that fulfill these requirements.

In particular, with respect to 3D image data at the cellular and subcellular scales, the axial resolution of a microscope limits the information obtainable from a given experiment. For example, despite its utility for acquiring single or multiple optically sectioned slices of often relatively flat cells, the axial resolution of confocal laser scanning microscopy (CLSM) is limited to approximately 600 nm with green emission probes and water immersion lenses (Pawley, 2010). In practice, in the presence of aberrations and when wide pinholes are

used for increased signal collection, the resolution is further lowered (Wilson, 1995), meaning that structures smaller than 600 nm cannot be resolved in the axial dimension. Spinning disk confocal microscopy, while better suited for live cell imaging, typically has an even worse axial resolution than CLSM (Wang et al., 2005). Point scanning microscope designs offer slightly improved resolution compared with spinning disk confocal designs but at the cost of reduced acquisition frame rates.

Light sheet fluorescence microscopy (LSFM) enables the imaging of cells and multicellular structures millimeters deep within large 3D samples (Ahrens et al., 2013; Huisken et al., 2004; Keller, 2013), but light sheets generated by Gaussian beams require a trade-off between image volume and axial resolution. Gaussian beams that are ~100 μm in length in the propagation direction yield an axial resolution of ~5 μm. Thus, although the early light sheet microscopes proposed by Stelzer and colleagues have been instrumental in revealing patterns of cell division and phenotype formation during development of a live organism (Huisken and Stainier, 2009; Keller et al., 2008, 2010; Pampaloni et al., 2007; Verveer et al., 2007), such Gaussian LSFM approaches cannot be used to measure subcellular signaling and detailed morphological features with isotropic, submicrometer resolution. Fusing multiple data stacks acquired under multiple viewing directions can reduce resolution anisotropy, however at the cost of reduced temporal resolution and more sample exposure (Swoger et al., 2007; Verveer et al., 2007). Alternative approaches such as lattice or Bessel beam LSFM can overcome these resolution limits (Chen et al., 2014; Fahrbach et al., 2010; Gao et al., 2012; Planchon et al., 2011) while still enabling rapid data acquisition, but introduce a new trade-off between beam propagation length and excitation confinement; in such systems relatively short beams are typically employed to resolve subcellular structures in great detail but they cannot image large samples in all three dimensions without sacrificing either excitation confinement or axial resolution. Because of these limitations in imaging volume, such approaches require samples that are constrained in at least one dimension, which is often achieved by exploiting the tendency of cells to spread into thin shapes on coverslips. This practice enforces very specific environmental constraints on the cells and is thus not suitable for the study of interactions between cells and their microenvironment.

Here, we report the development of an approach that fulfills the following performance criteria: (1) simultaneous imaging at multiple scales ranging from near-diffraction-limited structures (~300 nm) to spatially extended cells, small multicellular spheroids, and the large-scale environmental features that surround cells (100 μm); (2) temporal sampling at speeds sufficient to describe dynamic cell signaling events (~1 s); (3) cell environments that are not perturbed by proximity to glass coverslips or other non-physiological surfaces; and (4) nearly isotropic resolution that does not distort imaging of cell structure or signaling. Since our approach facilitates the quantitative study of intracellular processes in more realistic and precisely controllable microenvironments, we term it microenvironmental selective plane illumination microscopy (meSPIM). The 3D quantitative analysis enabled by this approach will open up the study of cell signaling and behavior in diverse but mechanically and chemically well-defined 3D microenvironments.

DESIGN

A Microscope Designed for Multiscale Isotropic Imaging of Subcellular Biology in 3D

The use of propagation invariant beams (Chen et al., 2014; Dean and Fiolka, 2014; Fahrbach et al., 2010; Planchon et al., 2011; Vettenburg et al., 2014) in LSFM enables high axial resolution over large fields of view, however more out-of-focus excitation is introduced with increasing beam propagation length as excitation confinement is gradually lost (Figures 1A and 1B). We define excitation confinement as the in-focus excitation intensity (or intensity squared in the case of two-photon excitation), i.e., excitation occurring within the depth of focus of the detection objective, relative to the total excitation intensity contained in the light sheet. For example, a one-photon Bessel beam with a 100-μm propagation length produces a light sheet with an excitation confinement of only 5% (Figure 1A). This lack of confinement leads to increased photobleaching and out-of-focus blur, complicating numerical post processing. Thus, a careful balance between propagation length (and hence field of view), resolution, and acceptable beam confinement must be found for each specific application. The combination of two-photon excitation with Bessel beam illumination (Planchon et al., 2011) can overcome the aforementioned shortcomings. The nearly ideal light sheets produced by this method (Figure 1B) confine the excitation power to the focal plane, have excellent axial resolution, and (theoretically) impose no limitations on the field of view. An experimentally tractable Bessel beam of 100 μm in propagation length results in an excitation confinement of 51% (Figure 1B).

Although out-of-focus fluorescence is minimal for sparse samples, such as isolated cells, for large and densely labeled samples, such as clusters of cells, some out-of-focus fluorescence is generated by the residual energy density in the beam skirt of the two-photon Bessel beam. We maintain high optical sectioning strength under these conditions by operating in "descanned mode," in which the lateral scan of the Bessel beam is synchronized with a rolling exposure of the sCMOS camera (Figures 1C and 1D). The effect is a confocal-type detection scheme (Baumgart and Kubitscheck, 2012; Fahrbach and Rohrbach, 2012; Fiolka et al., 2007) that rejects out-of-focus blur and offers increased robustness against aberrations. The two small side lobes and residual haze of the point spread function (PSF) in the axial direction are almost completely removed in the descanned mode (Figures 1E–1G), enhancing optical sectioning (Figure 1H). When meSPIM is operated in normal mode, we use linear deconvolution to remove the two small side lobes in the PSF, unless otherwise stated. To obtain high axial resolution over a large beam propagation distance, meSPIM employs a Bessel beam with an exceptionally high aspect ratio of 260 (Figure 1I), defined as the full width half maximum (FWHM) of the beam intensity profile along the propagation direction (96.8 μm) divided by the FWHM of its main lobe (372 nm). This design enables us to maintain near isotropic resolution in the range of 300–340 nm and uniform illumination over ~100 μm in the propagation direction of the beam (Figures 1J and 1K). Owing to a highly telecentric beam scanning system (i.e., the Bessel beam has a minimal angular

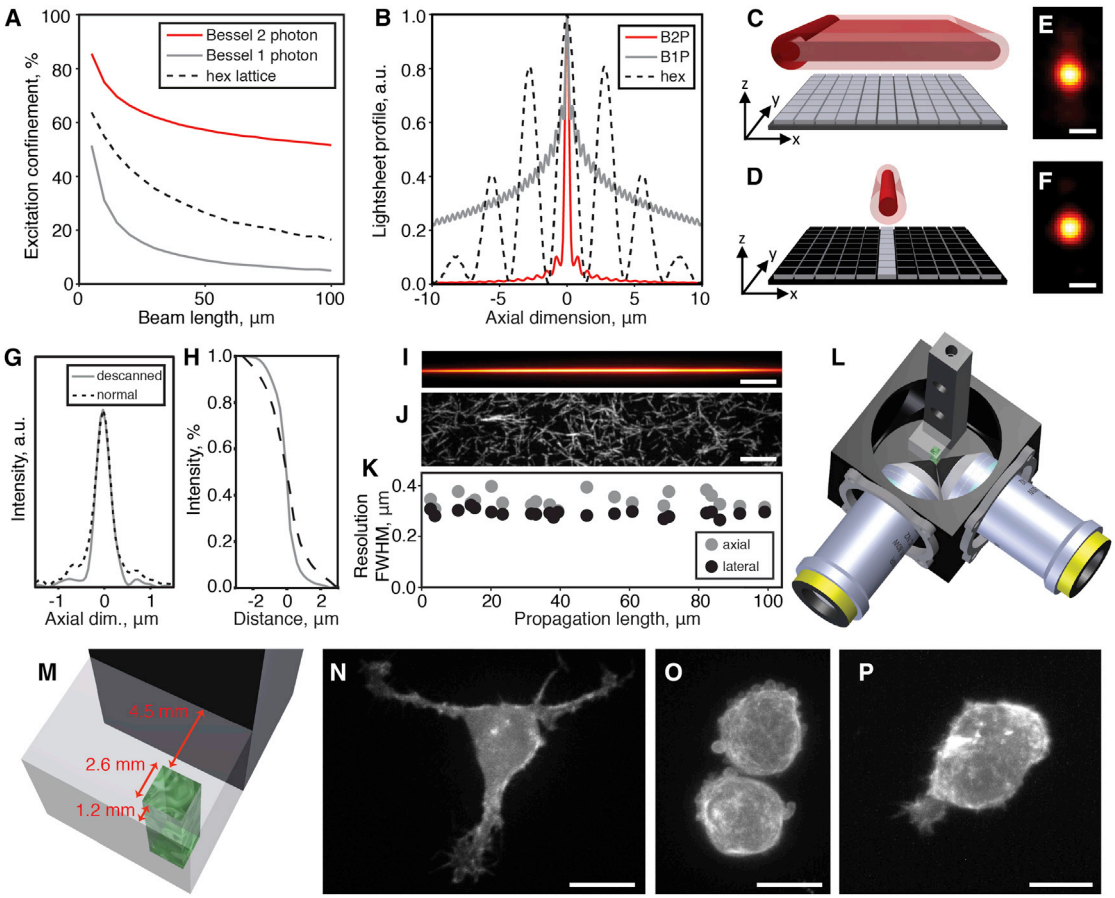

Figure 1. meSPIM Design Enables High-Resolution Imaging over Large Volumes in Controlled Microenvironments

(A and B) Simulation of the excitation confinement (A; percentage of excitation intensity contained within the depth of focus of the detection objective [1.1 μm] relative to total excitation intensity of a light sheet; squared intensity values are applied for two-photon excitation) for one-photon Bessel beam LSFM (Planchon et al., 2011), two photon Bessel beam LSFM (Planchon et al., 2011), and hexagonal lattice LSFM (Chen et al., 2014) for a beam propagation length of 100 μm and (B) the corresponding axial intensity profiles.

(C) Operating principle of the meSPIM normal mode: a Bessel beam (solid red) is rapidly scanned laterally to synthesize a time-averaged sheet of light (light red), and all camera pixels are exposed simultaneously (bottom, light gray).

(D) Operating principle of the meSPIM descanned mode: only a subset of pixels encompassing the image of the main lobe of the Bessel beam are active (bottom, light gray). This region is scanned synchronously with the Bessel beam to form a 2D image.

(E–G) Axial cross-sections of the raw image volume, i.e. no deconvolution, of a 100 nm bead in the normal (E) and descanned (F) mode along with corresponding axial profiles (G). Image data are resampled (3×) by zero padding of the Fourier transform of the bead images. Scale bars, 0.5 μm

(H) Axial sectioning of a human bronchial epithelial cell (HBEC) spheroid expressing eGFP-Kras^{V12} in the normal and descanned modes.

(I) Stationary two-photon Bessel beam as imaged in an aqueous fluorescein solution. Scale bar, 10 μm.

(J) xz cross-section, obtained by summing two adjacent image slices, of collagen labeled with CNA35 peptide conjugated to Cy5 dye imaged in normal mode. Scale bar, 10 μm.

(K) Measurement of meSPIM resolution in the axial and lateral dimensions, given as the FWHM of 200-nm fluorescent beads. See also Figure S1.

(L) Rendering of the microscope sample holder and objective geometry.

(M) Detailed rendering of the sample holder consisting of an aluminum beam (black) and an agarose cube (light gray) that contains the collagen sample (green).

(N) Non-deconvolved xy maximum intensity projection over the entire cellular volume of a primary melanoma cell expressing GFP-tractin embedded in collagen near a glass coverslip and imaged using a spinning disk confocal microscope.

(O) Non-deconvolved xy maximum intensity projection over the entire cellular volume of two primary melanoma cells expressing GFP-tractin and from the same tumor as the cell in (M).

(P) Non-deconvolved xy maximum intensity projection over the entire cellular volume of a primary melanoma cell expressing GFP-tractin embedded in collagen crosslinked with 3 mM ribose.

The cells in (O) and (P) are embedded in 2.0 mg/ml collagen far from any hard surfaces and were imaged using meSPIM in non-descanned mode. Scale bars, 10 μm (N, O, and P).

deviation during lateral and axial scanning), shift invariant imaging can be maintained over large volumes (Figure S1). In summary, the microscope design proposed here enables imaging of image volumes of up to 160 × 160 × 100 μm^3 with shift invariant, nearly isotropic resolution of ~300 nm, high signal to noise ratio and very low background haze.

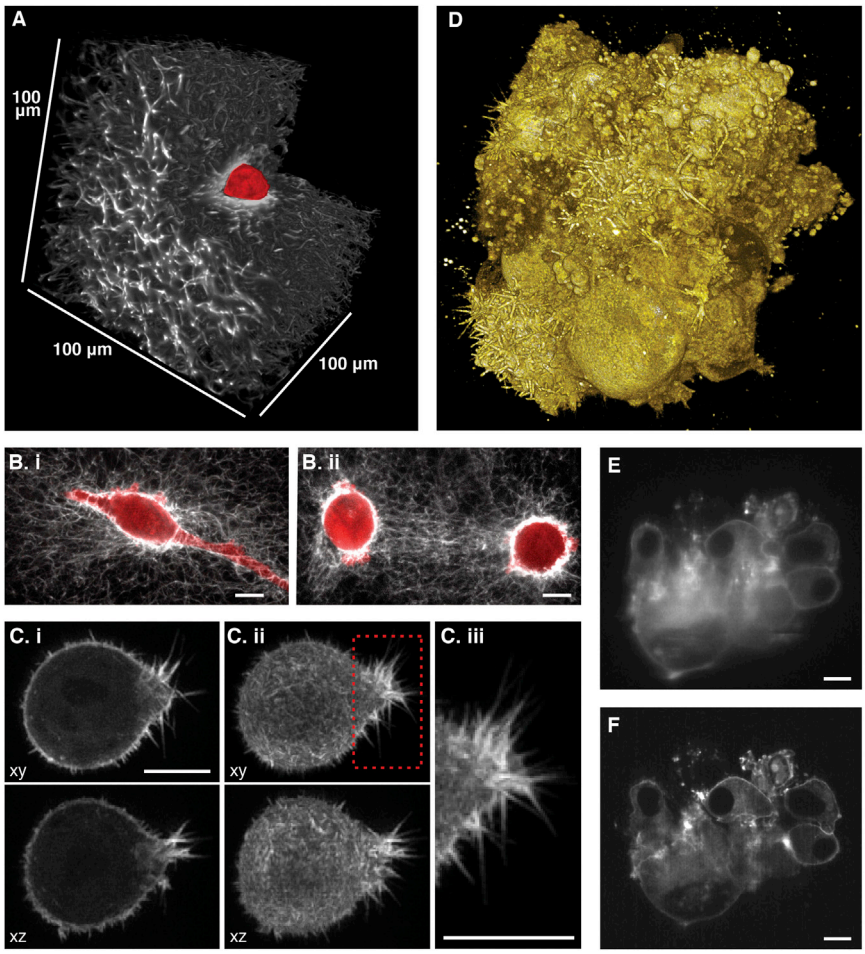

Figure 2. meSPIM Enables Imaging of Fine, Subcellular Features over Large Image Volumes

(A) 3D volume rendering of a single melanoma cell in a cubic volume measuring 100 μm on each side (Movie S1). The cell is labeled with cytosolic GFP and the collagen I matrix was labeled with CNA35 conjugated to Cy5. Neither the GFP nor the collagen channel are deconvolved.

(B) xy maximum intensity projections of MV3 cells over 3 μm about the equatorial plane.

(C) Deconvolved images of transformed HBEC expressing GFP-tractin in a collagen I matrix. (i) Cross-sectional views in the xy and xz planes are obtained via maximum intensity projections over 2 μm about the equatorial plane. (ii) Maximum intensity projections over the entire image volume of the same cell (Movie S1). (iii) Magnified view of the boxed region in (ii).

(D) 3D volume rendering of transformed HBEC cells expressing eGFP-Kras^{V12}; image volume acquired in descanned mode (Movie S1).

(E) Non-descanned, non-deconvolved xz cross-section obtained by summing two adjacent slices.

(F) Descanned, non-deconvolved xz cross-section obtained by summing two adjacent slices.

Scale bars, 10 μm.

Effects of 2D and 3D Microenvironments on Cell Morphology

It is well documented that cells behave very differently in 3D microenvironments than on 2D surfaces, and even embedded within a 3D matrix, cells behave differently when in proximity to a glass coverslip or other stiff surfaces (Ma et al., 2013; Provenzano et al., 2009; Rao et al., 2012; Wang et al., 2014). To enable the controlled study of the effects of matrix mechanical properties on cell function (Rao et al., 2012), we therefore designed meSPIM to image cells in microenvironments free of hard surfaces near the sample (Figures 1L and 1M). Imaging cells in such unperturbed microenvironments, we noticed striking morphological differences in cells in 3D collagen near glass. For example, primary melanoma cells near glass exhibit stretched and branched morphologies dominated by actin-based protrusions (Figures 1N and S2), whereas identical cells far from any stiff surface exhibit rounded morphologies dominated by blebbing (Figure 1O). This observation suggests that microscope design limitations may have distorted much of our current understanding of subcellular spatial organization. We determined that this morphological shift is due at least in part to matrix stiffness by increasing the stiffness of the collagen matrix by using ribose to crosslink collagen fibers (Girton et al., 2000; Roy et al., 2010). Embedded within cross-linked collagen, cells exhibit abundant actin-driven protrusions (Figure 1P) but do not generally exhibit the same stretched morphologies as cells near glass. These observations highlight the need for imaging methods that allow the study of cell morphology and behavior in mechanically unconstrained microenvironments. We envision that the microenvironmental control facilitated by meSPIM will also enable the analysis of cellular- and subcellular-scale mechanisms that couple cell behavior to the microenvironment.

RESULTS

Multiscale Imaging Enables Simultaneous Observation of Subcellular Features and the Microenvironment

Using meSPIM, we simultaneously imaged cells and their surrounding collagen matrix over large fields of view (Figure 2A; Movie S1). These images show how in 3D microenvironments cells can extend in any direction (Figure 2Bi) and can interact with their environment over long distances (Figure 2Bii). With the same optical configuration, we were also able to image very fine cell morphological structures, such as the highly dynamic filopodia present on transformed human bronchial epithelial cells (HBEC; Figure 2C and Movie S1).

Interactions with other cells are a major component of the cellular microenvironment. We therefore evaluated meSPIM's ability to simultaneously image multiple interacting cells. Large samples, such as cancer cell spheroids, are particularly sensitive to out-of-focus blur. However, the descanned mode enabled us to drastically enhance the image clarity of large 3D cancer cell spheroids while simultaneously capturing the wide morphological heterogeneity at the single cell level (Figure 2D

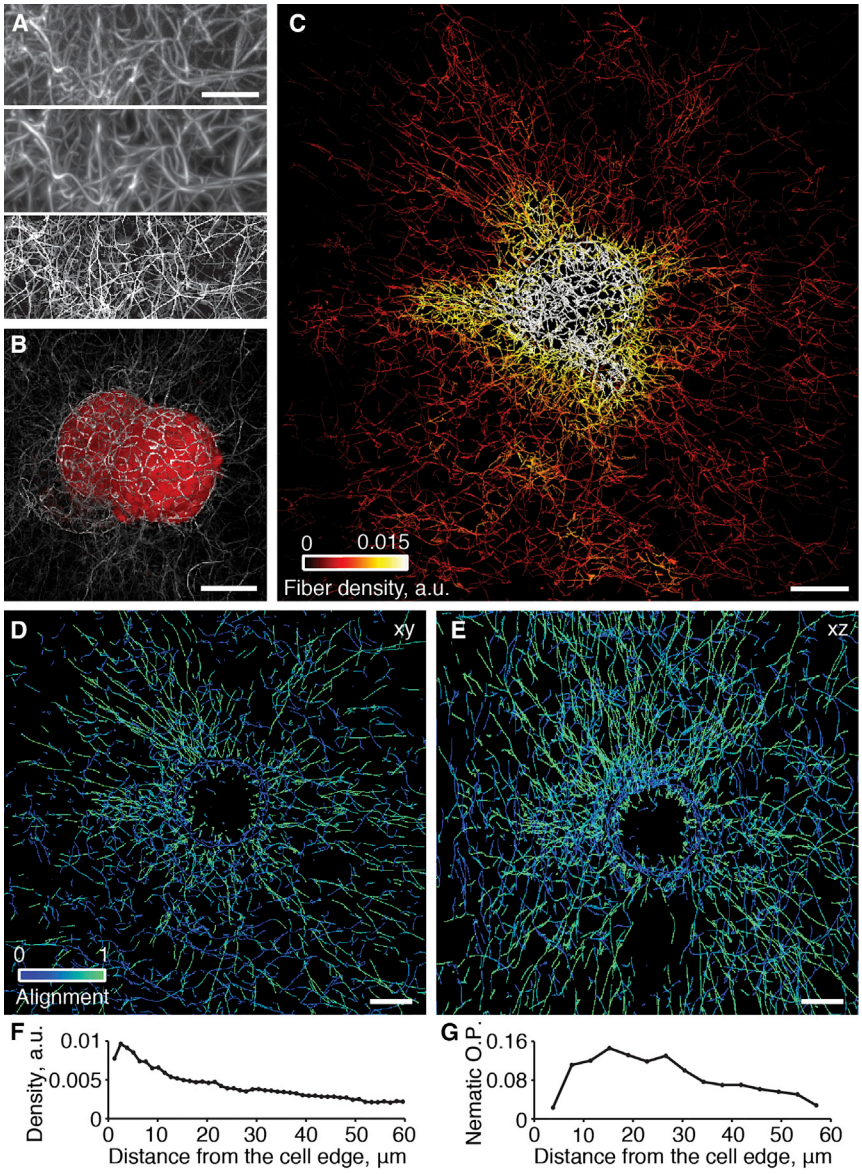

Figure 3. meSPIM Combined with Computer Vision Enables Imaging, Visualization, and Quantification of How Cells Alter Collagen Fibers over Large Distances within an Image Volume Measuring 100 μm on Each Side

(A) xy maximum intensity projections over 12 μm showing single collagen fibers labeled with CNA35 peptide conjugated to Cy5 dye imaged in normal mode (top), output of the steerable filter algorithm showing the filter response (middle), and central locations (non-maximum suppressed) of collagen fibers (bottom) (Movie S2).

(B) 3D volume rendering of two melanoma cells (red) and the central locations of collagen fibers (grayscale).

(C–E) Normalized fiber density (averaged over 2 μm) surrounding the single MV3 cell in Figure 2A shown as a 3D rendering of the xy view over the minimum axial distance necessary to encompass the cell (C; Movie S2). Fiber alignment relative to the vector pointing toward the cell center, shown as (D) xy and (E) xz maximum intensity projection over 12 μm.

(F) Mean fiber density over the entire image volume as a function of distance from the cell edge.

(G) Nematic order parameter as a measure of fiber alignment toward the cell center. A value of 1 indicates perfect alignment toward the cell center and 0 indicates random alignment.

Scale bars, 10 μm.

and Movie S1). Compared with the normal mode (Figure 2E), the descanned images (Figure 2F) show greatly reduced out-of-focus blur, improved optical sectioning strength, better maintenance of resolution throughout the sample, and have a dramatically increased signal to background ratio, allowing us to observe eGFP-KRas^{V12} enrichment in the cell membrane that was obscured in the normal mode.

Automated 3D Image Analysis of Fibrous Microenvironments

In fibrous 3D microenvironments, cells interact with individual fibers at the submicrometer scale but also deform and modify the ECM over scales of hundreds of micrometers (Provenzano et al., 2006; Rubashkin et al., 2014; Shi et al., 2014). Although the molecular mechanisms that regulate this phenomenon have been studied qualitatively (Brownfield et al., 2013; Thievessen et al., 2015), meSPIM allowed us to develop an automated algorithm that uses 3D steerable filters (Aguet et al., 2005; González et al., 2009; Jacob and Unser, 2004) to measure the locations and orientations of individual collagen fibers throughout the relatively large volumes that form the cellular microenvironment (Figure 3A and Movie S2). Detecting individual fibers also improves visualization of the dense collagen network formed near cells (compare Movie S1 with Movie S2), allowing us to visualize cellular blebs that protrude through a dense collagen mesh (Figure 3B).

Although collagen fiber alignment appears to affect tumor cell invasion (Conklin et al., 2011), it remains unclear to what extent the observed cellular manipulation of collagen in vitro is due to microscope limitations. Here, we confirm that cells can manipulate collagen fibers over large distances in the absence of any rigid surfaces, and we further quantified the distance over which fiber manipulation propagates through such a collagen gel. Cells increased the local density of fibers (Figure 3C and Movie S2), and our 3D quantitative analysis revealed regions of dense collagen fibers, suggesting that prior to imaging a cell protruded, bound to collagen fibers, and then retracted to create patches of increased collagen density. Cells also reoriented individual collagen fibers. Our analysis of local fiber alignment shows that, immediately adjacent to the cell surface, fibers are wrapped around the cell, whereas fibers further from the cell surface are aligned toward the cell center (Figures 3D and 3E). Our 3D steerable filter analysis shows that these fiber alignment and local

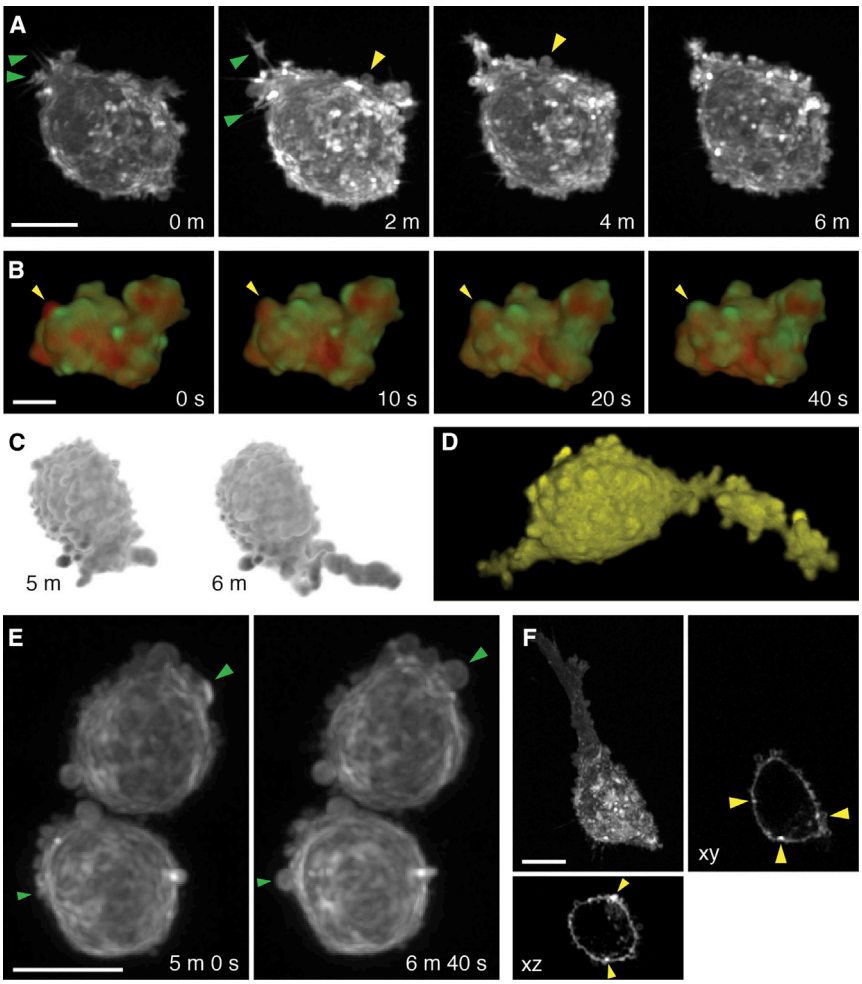

Figure 4. meSPIM Enables Detailed Imaging of the Morphological Diversity of Melanoma Cells in Mechanically Unperturbed 3D Microenvironments

(A) Maximum intensity projection of an MV3 cell expressing GFP-tractin. Green arrowheads indicate actin-rich filopodia and yellow arrowheads indicate non-apoptotic membrane blebs.

(B) 3D volume rendering of an MV3 cell expressing CyOFP-tractin and cytosolic GFP. Emergence of an actin-free membrane bleb and ensuing accumulation of actin in the newly formed membrane protrusion are indicated by arrowheads (Movie S3).

(C) A 3D volume rendering of a rapid protrusion event in a primary melanoma cell expressing cytosolic GFP (Movie S3).

(D) A 3D volume rendering of stable protrusive structures and sustained blebbing in a primary melanoma cell expressing cytosolic GFP (Movie S3).

(E) xy maximum intensity projections (over the entire image volume) of primary melanoma cells expressing GFP-tractin (Movie S3). Arrowheads indicate the emergence of new blebs. The first time point of this time lapse acquisition is shown in Figure 1O.

(F) xy maximum intensity projection over the entire image volume along with xy and xz cross-sections of an MV3 cell expressing a membrane marker consisting of td-Tomato fused to the first 60 base pairs of GAP43 (Figure S4). Arrowheads indicate local enrichment of the plasma membrane.

Scale bars, 10 μm.

density modifications decay with increasing distance from the cell (Figures 3F and 3G). Such reorganization of collagen fibers by cells was abolished by inhibiting myosin II contractility using blebbistatin, which suggests that these manipulations result from intracellular contractility (Figure S3). In summary, these two examples demonstrate how we can leverage the large ratio between sample volume and spatial resolution to dissect the mechanical interactions between cells and their microenvironment.

Control over the Microenvironment Enables Observation of Spontaneous and Ubiquitous Pressure-Based Protrusions

The ability to image fine cellular details in controllable microenvironments revealed morphodynamic features not commonly observed in the narrow range of mechanical environments usually studied in vitro. For example, human melanoma cells switched rapidly between filopodial structures and membrane blebs (Figure 4A). In fact, when we imaged melanoma cells deep within collagen gels without extensive cross-links between fibers, cellular blebbing appeared as the predominant morphodynamic feature and cells survived and continued blebbing for several days under these conditions. Although the biophysical and molecular aspects of blebbing have been described, many of these studies have used melanoma cells that were depleted of filamin, presumably to encourage blebbing under artificial conditions (Charras et al., 2005, 2006, 2008). Our observation that melanoma cells can bleb spontaneously without any genetic or protein perturbations suggests that blebbing is an inherent feature of melanoma cells. Furthermore, our observation that blebbing in melanoma cells depends on matrix stiffness suggests that cells can sense the stiffness of their environment and that blebbing may be a response to soft microenvironments. For example, such non-apoptotic blebs are hypothesized to mediate morphodynamic rearrangements in cells occupying non-rigid environments such as tissue and purified collagen (Fackler and Grosse, 2008; Paluch and Raz, 2013). Simultaneous dual color imaging confirmed that these protrusive structures begin as actin-free blebs but then fill with actin that concentrates in the newly protruded membrane region (Charras, 2008; Charras and Paluch, 2008) (Figure 4B and Movie S3). Using this pressure-driven protrusion mechanism, cells can create large protrusions very quickly (Figure 4C and Movie S3). Bleb-based protrusions sometimes stabilized after filling with actin, after which blebbing continued stochastically throughout the cell (Figure 4D and Movie S3). Although the frequency of bleb stabilization is relatively low, this phenomenon may be the basis for bleb-based motility (Diz-Muñoz et al., 2010; Liu et al., 2015; Ruprecht et al., 2015). Indeed, we observed melanoma cells blebbing persistently with a strong spatial bias (Figure 4E and Movie S3), which may enable cell migration through dense but deformable ECM microenvironments.

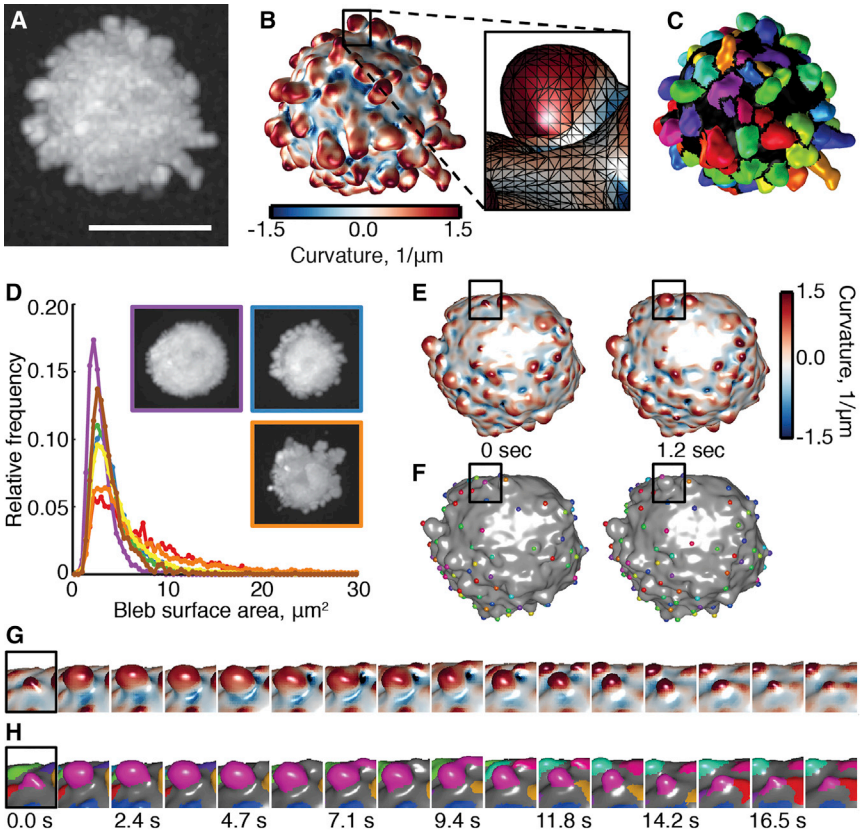

Figure 5. meSPIM Combined with Computer Vision Enables the Automated Detection and Tracking of Dynamic 3D Morphological Structures

(A) xy maximum intensity projection (over the entire image volume) of a primary melanoma cell expressing cytosolic GFP.

(B) Surface curvature of the cell shown in (A). Inset shows the triangularized mesh that represents the cell surface.

(C) High-curvature surface structures (blebs) identified by segmentation and region merging (Movie S4).

(D) Frequency distributions of bleb surface areas on six different cells (see also Figure S5). Inset: maximum intensity projections of cells corresponding to the color-matched frequency distributions.

(E) 3D surface renderings of mean curvature from a rapid time lapse series (1.2 s per image volume).

(F) Automated tracking of individual blebs; colors indicate separate tracks (Movie S4).

(G) Close-up of the region indicated in (E), showing the entire lifecycle of a single membrane bleb.

(H) Close-up of the region indicated in (F), showing individually tracked blebs encoded by color.

Scale bar, 10 μm.

In addition to enabling motility, membrane blebs may influence diverse cell signaling pathways by regulating membrane and actin microdomains (Dinic et al., 2013; Laser-Azogui et al., 2013). For example, when the actin-filled structures retracted instead of stabilized, they left behind patches of elevated actin concentration, sometimes called actin scars (Figure 4E). Use of a non-specific membrane marker also revealed elevated membrane concentration in some areas, suggesting that expansion and wrinkling of the cell membrane itself may occur in these regions (Figure 4F). Simultaneous imaging of two different membrane-localized fusion proteins confirmed that these patches of increased membrane concentration are not due to fusion protein aggregation (Figure S4). Such compression and dilation of the membrane have been observed previously, albeit in much larger areas (Kapustina et al., 2013). Given the involvement of actin and membrane-localized proteins in cell signaling (Goswami et al., 2008; Harding and Hancock, 2008), it seems plausible that these patches may play a role in organizing cell signaling events.

Automated 3D Image Analysis of Bleb Sizes and Dynamics

Visualizing 3D data can be cumbersome and identifying the temporal and spatial properties of subcellular structures in 3D is difficult if not impossible via manual identification and tracking (Driscoll and Danuser, 2015); this fact is exacerbated by the quantity of data generated by meSPIM. Here, we demonstrate that meSPIM produces images of sufficient quality to identify and track blebs, which are relatively small and short-lived compared with other protrusion types, in an automated and high-throughput fashion.

The nearly isotropic resolution of meSPIM simplifies the development of quantitative analyses and facilitates the application of techniques that were originally designed for 2D image analysis or computer graphics. We developed a bleb detection workflow that uses a computer graphics algorithm, which was in turn based on an algorithm from 2D image analysis (Mangan and Whitaker, 1999). This workflow calculates the local surface curvature of cells and uses watershed segmentation to identify regions of high curvature as blebs (Figures 5A–5C and Movie S4). Comparison with manual bleb identification shows that this algorithm performs well for bleb identification using meSPIM data (see Experimental Procedures). Using identical analysis and imaging conditions, we quantified the sizes and shapes of every bleb on seven different cells, revealing systematic cell-to-cell variation in the surface area of blebs. This observation suggests that differences in cell state can have global effects on distributed subcellular structures such as blebs (Figure 5D). We further analyzed the distribution of bleb sizes in two different melanoma cell lines (Figure S5). In addition to demonstrating the robustness of our imaging pipeline and software for identifying and quantifying morphological features, these results illustrate how bleb size and density vary across cells. By leveraging the rapid imaging capabilities of meSPIM we were also able to automatically identify and track (Jaqaman et al., 2008) individual membrane blebs as they appeared and disappeared (Figures 5E–5H and Movie S4) at a volume sampling rate of ~1 Hz.

3D Isotropic Resolution Enables Quantification of Protein Localization and Activity in Live Cells

The ability to measure protein localization and activity in single living cells is critical to our understanding of cell fate decisions,

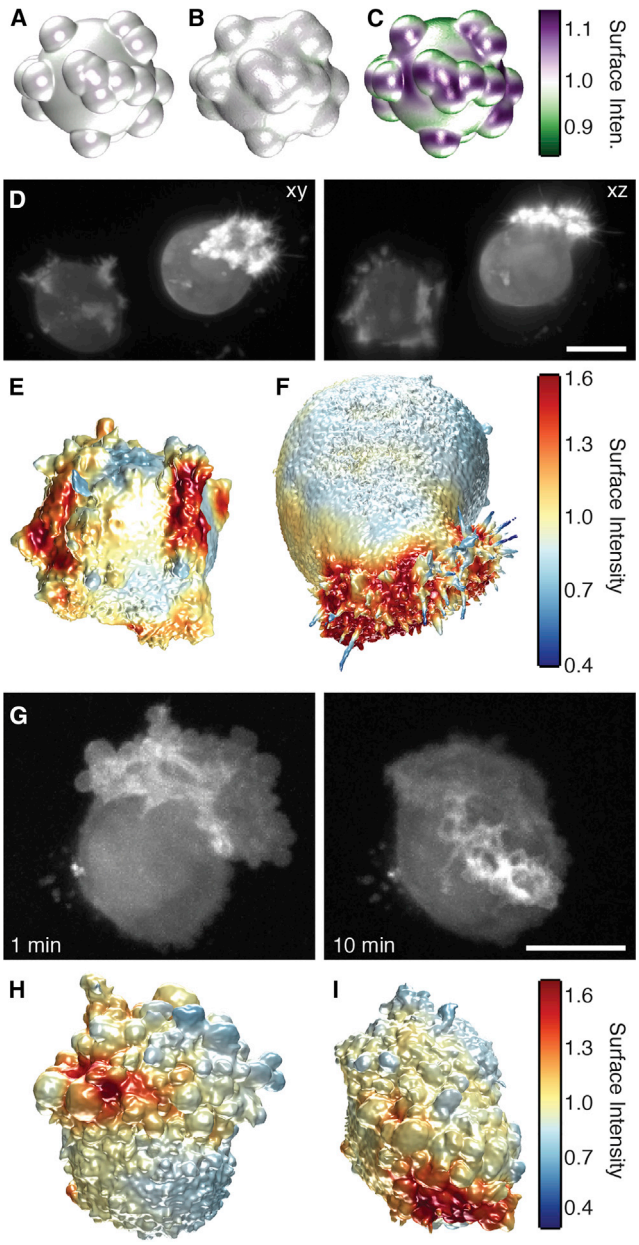

Figure 6. Nearly Isotropic Resolution of meSPIM Enables Quantification of Protein Intensity on the Cell Surface

(A–C) Intensity measured on the surface of a simulated, uniformly cytosolically labeled cell imaged with (A) isotropic resolution, (B) worse isotropic resolution, (C) and asymmetric resolution with axial resolution as in (B) and lateral resolution as in (A). Note that surface intensity in (A)–(C) all share the same color map, shown on the far right.

(D) Maximum intensity projections of two HBEC cells expressing GFP-tractin. Because of the high dynamic range, both images were gamma corrected with a gamma of 0.6.

(E and F) The surfaces of these two cells are shown colored by the local concentration of actin within a 1-μm radius.

(G) Maximum intensity projections at two time points of a melanoma cell (MV3) embedded in crosslinked collagen and expressing GFP-AktPH, a PI3K activity biosensor.

(H and I) The surfaces at these two times are shown colored by the local concentration of AktPH within a 1-μm radius.

Scale bars, 10 μm.

yet most microscopy approaches yield data that are ill-suited for making quantitative conclusions regarding protein localization. The inaccurate localization of fluorescent proteins is apparent from simulations showing how a spatially homogeneous signal is affected by isotropic blur of different magnitudes (Figures 6A and 6B) compared with equivalent observations of the same signal convolved with an axially stretched PSF that approximates that obtainable by spinning disk confocal microscopy (Figure 6C). Accuracy in measuring protein localization is especially important for proteins that reside on or near the cell membrane. For example, we observe that actin resides almost exclusively in the cell cortex for cells in 3D microenvironments (Figure 2), and meSPIM enabled us to quantify the local concentration of actin near the surface of HBEC cells that formed different types of actin-rich protrusions (Figure 6D). One cell presented numerous dynamic actin-rich regions that moved around the cell (Figure 6E), whereas the nearby cell presented a single more stable but highly enriched actin area from which numerous diffraction-limited filopodia emerged (Figure 6F). This observation highlights both the resolution and quantitative capabilities of meSPIM, and suggests that under these conditions, a very dense actin region may stimulate local formation of filopodia.

In addition to direct protein localization, protein activity biosensors provide invaluable insight into the subcellular dynamics of signal transduction. For example, translocation biosensors indicating the local concentration of phosphoinositides on the cell membrane have been used to quantify activity of proteins such as phosphatidylinositol 3-kinase (PI3K) and protein kinase C (Teruel and Meyer, 2000). Such translocation biosensors, however, require the ability to resolve membrane-associated proteins from those residing in the cytosol, which is not possible in the axial dimension of images obtained using confocal microscopy. This requirement has to date only been achieved by total internal reflection fluorescence (TIRF) microscopy, which requires that cells are adhered to a glass coverslip and thus cannot be used to image cells in 3D microenvironments. meSPIM facilitates the use of translocation biosensors in 3D by enabling us to resolve membrane-associated (active) biosensor from cytosolic (inactive) biosensor signals. For example, we quantified PI3K activity in MV3 melanoma cells using the GFP-AktPH biosensor (Haugh et al., 2000), revealing dynamic regions of high PI3K activity that move around the cell (Figure 6G). When comparing the maximum intensity projections in Figure 6G with the surface intensity data in Figures 6H and 6I, it is important to note that the regions of high PI3K signaling in Figure 6G may reside anywhere within the cell; in contrast, Figures 6H and 6I show only PI3K activity localized to the cell surface. This phenomenon of PI3K "hotspots" has been associated with persistence and reorientation of fibroblasts migrating on 2D surfaces (Melvin et al., 2011; Weiger et al., 2010; Welf et al., 2012), but the role of PI3K signaling in cells occupying 3D microenvironments remains to be explored. Our approach enables this and many other investigations utilizing such translocation biosensors.

DISCUSSION

Here we demonstrate optical and computational tools specifically to facilitate quantitative study of how cells function in more physiological conditions, and in doing so we also directly

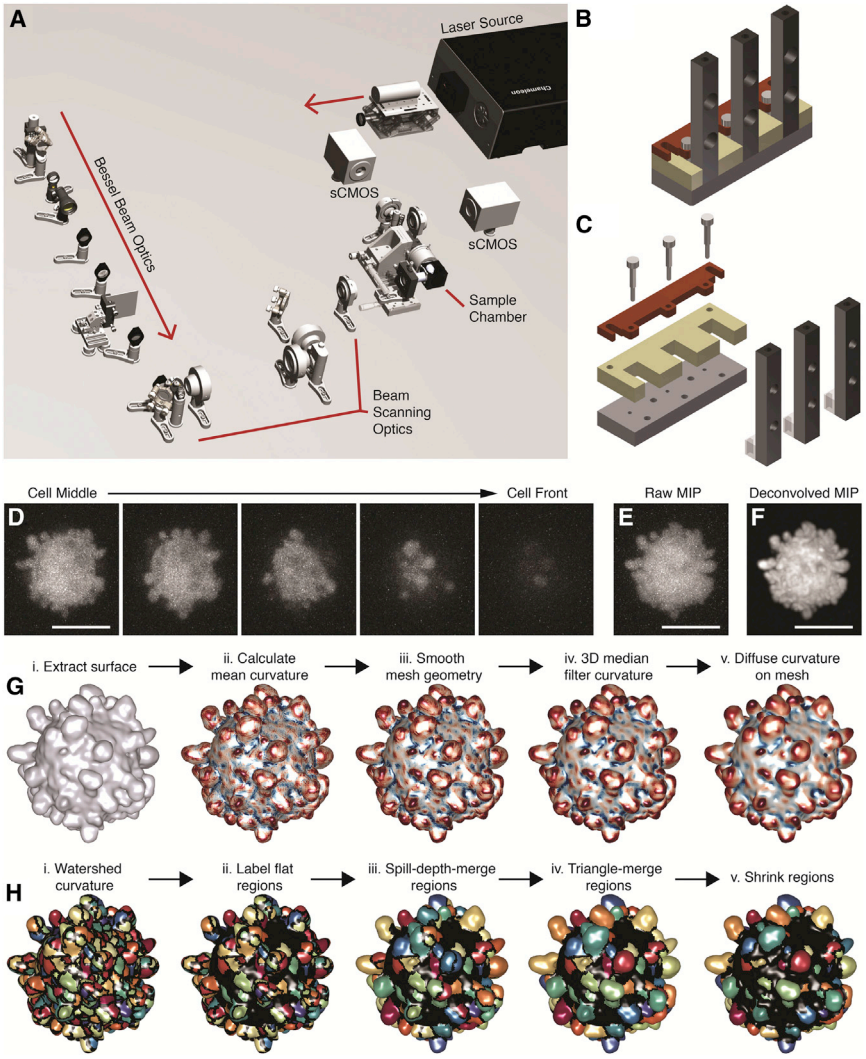

Figure 7. meSPIM Design and Bleb Segmentation Workflow

(A) Detailed rendering of the meSPIM optical train (its components are described in detail in the microscope components folder within the meSPim Supplemental Information zip file).

(B and C) Mold for casting the agarose sample holder and sample mounting apparatus.

(D–H) Bleb segmentation workflow. (D) xy maximum intensity projections of the undeconvolved image over consecutive depths of 2 μm from the middle to the front of the cell. (E) xy maximum intensity projection over the entire cell. (F) xy maximum intensity projection over the entire cell of the deconvolved image. (G, i) The cell surface is extracted from the deconvolved image. (ii, iii) The mesh that represents the cell surface is smoothed and the mean surface curvature calculated. (iv) Curvature is median filtered in 3D and (v) then further smoothed by allowing it to diffuse over the surface. (H, i) To segment blebs, smoothed curvature is next segmented using a watershed algorithm, and (ii) flat regions, shown black, are labeled. (iii) Regions are next iteratively merged using a spill-depth criterion and then (iv) iteratively merged using a triangle criterion. (v) Finally, regions can be shrunk for visualization.

Scale bars, 10 μm.

address issues of data handling and sample mounting that have been previously raised as impediments to widespread adoption of LSFM (Reynaud et al., 2015; Stelzer, 2015) (see also Figure 7). We find that cells in the unperturbed 3D conditions used here exhibit morphological features that have been described sparingly in the literature but may represent crucial phenotypes in vivo. Such features have not been readily observable or quantifiable, possibly because the required resolution has heretofore been achieved only when samples are imaged near a glass coverslip. Our observations of melanoma cells appear strikingly different from the same cells allowed to adhere to glass coverslips. For example, we have not observed the thick actin bundles commonly referred to as stress fibers using this microscopy approach, raising the concern that many of the accepted features of cell morphology and function may be artifacts of routine sample preparation and imaging approaches. Cells in 3D microenvironments adopt mainly rounded morphologies that resemble in vivo observations (Blaser et al., 2006; Gligorijevic et al., 2014) and exhibit bleb-based protrusions that may facilitate an important cell motility mechanism in soft matrices.

Cell biology is necessarily restricted to studying what we can measure. Accordingly, while the last hundred years have yielded incredible insight into cellular processes, unfortunately most of these studies have involved cells plated onto flat, stiff surfaces that are drastically different from the in vivo microenvironment. Thus, although the effects of the 3D microenvironment on cell function have been appreciated for some time, we have yet to create experimental approaches that enable us to measure detailed subcellular structures and signaling events in cells occupying 3D microenvironments that are free from proximity to hard surfaces. Similarly, we have a vague notion of how the mechanical properties of the 3D microenvironment regulate cell signaling and cell fate, but technical limitations have so far prevented systematic study of how the forces cells place on a flexible microenvironment are turned into signals that affect cell state. Here, we introduce an imaging platform that enables detailed subcellular observations without compromising microenvironmental control and thus should open a window for addressing these fundamental questions of cell biology.

LIMITATIONS

3D image analysis at the subcellular scale, although a necessary element of the light sheet microscopy workflow, remains challenging. In particular, the bleb segmentation algorithm presented here has difficulty distinguishing multiple blebs that have merged from irregularly shaped blebs. Bleb segmentation

quality would likely improve with manual bleb annotation, which would allow for the use of supervised machine learning techniques. However, with current visualization technology, the manual annotation of complex 3D data is time consuming, cumbersome, and may suffer from user bias. Also, correctly measuring the fluorescence intensity near cell surfaces or even measuring the locations of collagen fibers within a collagen network are only the initial steps in interpreting such complex data. Further methods, such as statistical methods for analyzing data defined on non-Euclidean manifolds like the cell surface, will need to be developed to render such complex data interpretable.

Although two-photon absorption in meSPIM enables excitation confined to the focal plane over large fields of view, this also comes with disadvantages: (1) the choice of fluorophores with suitable two-photon absorption cross-sections and fluorescence quantum yields is limited; (2) fluorophores with spectrally distinct two-photon absorption cross-sections require multiple ultrafast pulse trains (e.g., with an optical parametric oscillator) or slow tuning of the laser emission wavelength; and (3) intense laser pulses used for two-photon excitation can lead to accelerated photobleaching and phototoxicity. As designed, meSPIM excels at imaging large volumes with high spatiotemporal resolution. However, for small and thin samples, especially cells adherent to glass coverslips, other techniques like lattice light sheet microscopy may be operated with lower light dosages. In this regime where relatively short beams (~15 μm propagation length) can be employed, the out-of-focus beam skirt for high-resolution lattice patterns is reduced. Thus meSPIM excels for a class of samples that extend in all three dimensions over length scales on the order of 100 μm, such as the 3D microenvironments imaged in this work.

EXPERIMENTAL PROCEDURES

Microscope Design

A detailed illustration of the optical setup can be found in Figures 7A–7C and a detailed parts list and drawings of custom components as well as an instruction on the microscope alignment is located in the in the meSPim Supplemental Information zip file. Near infrared laser pulses (150 fs pulse length, 80 MHz repetition rate, wavelength 900 nm) from a Ti:Sapph oscillator (Chameleon Ultra II, Coherent) were expanded five times by a Galilean telescope and shaped to a Bessel beam by an Axicon (Thorlabs). Following an achromatic lens, the resulting ring-shaped intensity distribution in a Fourier plane was cleaned up with a custom-made photomask (Photosciences). The mask contained a series of thin annuli that varied slightly in inner and outer diameter to adjust the desired propagation length and optimize light transmission (around 70% for the design wavelength of 900 nm). The mask is necessary to clean up optical imperfections of the Axicon. The ring was imaged onto a first galvanometric mirror (Cambridge Technology), which scans the Bessel beam in the lateral plane. The ring image was further relayed with two telecentric scan lenses (Sill Optics) to a second galvanometric mirror (Cambridge Technology), which performed the axial scan, and was subsequently imaged into the backfocal plane of the illumination objective with a scan lens (Sill Optics) and a tube lens (ITL200, Thorlabs). Folding mirrors were used to very slightly adjust the rotation of the scan axes relative to the Cartesian axes that span the imaging volume.

Nikon NA 0.8/40X water dipping objectives were used for illumination and fluorescence detection, arranged orthogonally to each other. The detection objective was actuated by a piezo actuator (PiFOC, Physik Instrumente) to perform z-stepping for 3D image acquisition. Fluorescence light collected by the detection objective was split into a green and red channel by a dichroic mirror (Chroma) and imaged with tube lenses (ITL 200, Thorlabs) on two sCMOS cameras (Orca Flash II, Hamamatsu). Excitation light was blocked by two short-pass filters (Semrock).

Instrument control was performed by a custom written LabView code developed by Coleman Technologies. The initial software kernel was licensed from Howard Hughes Medical Institute's Janelia Farm (HHMI). The kernel was then substantially expanded by Coleman Technologies to suit our microscope and add additional functionalities such as the descanned mode. The entire code package can be requested for academic use from the corresponding authors and will be delivered under material transfer agreements with HHMI and UT Southwestern Medical Center. In the normal mode, the Bessel beam was laterally scanned five times using a triangular waveform during the acquisition of one image frame. In the descanned mode, the cameras were operated in the light sheet mode and a single scan of the Bessel beam, tightly synchronized to the camera readout, was performed during the acquisition of one image frame.

Cell Culture and Reagents

MV3 and A375 melanoma cells were cultured using DMEM (Gibco) supplemented with 10% fetal bovine serum (FBS) at 5% CO_2 and 21% O_2. Primary melanoma cells were cultured using the Primary Melanocyte Growth Kit (ATCC) at 5% CO_2. HBECs immortalized with Cdk4 and hTERT expression and transformed with p53 knockdown, $Kras^{V12}$, and cMyc expression (Sato et al., 2013) were cultured in keratinocyte serum-free medium (Gibco) supplemented with 50 mg/ml of bovine pituitary extract (Gibco), 5 ng/ml of EGF (Gibco), and 1% Anti-Anti (Gibco) in a humidified incubator at 5% CO_2, 2% O_2, and 37°C. To induce formation of tumor spheres, cells were seeded into ultra-low attachment round-bottom 96-well plates (Corning) at a density of 10,000–30,000 cells per well for 2–4 days before imaging.

The GFP-tractin construct contains residues 9–52 of the enzyme IPTKA (Johnson and Schell, 2009) fused to GFP (Yi et al., 2012). The CyOFP-tractin peptide contains the tractin peptide fused to the novel CyOFP protein. CyOFP is a cyan-excitable orange fluorescent protein with peak excitation at 505 nm and peak emission at 588 nm, details of which will be described in a separate article currently in preparation. The td-Tomato membrane marker contains td-Tomato fused to the first 60 base pairs of GAP43 (neuromodulin). The GFP membrane marker contains GFP fused to the 20-amino acid farnesylation signal from c-Ha-Ras (Kanchanawong et al., 2010). The GFP-$Kras^{V12}$ plasmid was constructed by cloning a $Kras^{V12}$ fragment from the pLenti-$Kras^{V12}$ construct (Sato et al., 2013) into the pLVX-GFP vector (Clontech). Fluorescent protein constructs were expressed in cells using the pLVX lentiviral system (Clontech) according to the manufacturer's instructions, except for the GFP membrane marker, which was expressed using Lipofectamine (Invitrogen). The collagen matrix was labeled with the collagen-binding peptide, CNA35 (Xu et al., 2004), that had been expressed in *Escherichia coli*, purified, and fluorescently tagged using N-hydroxysuccinimide-ester chemistry (Cy5, Amersham).

Collagen gels were created by mixing either rat tail collagen I (Corning) or bovine collagen I (Advanced Biomatrix) with concentrated PBS and water to create gels of either 2.4 mg/ml or 2.0 mg/ml, respectively. This collagen solution was then neutralized with 1 N NaOH and mixed with cells just prior to incubation at 37°C to induce collagen polymerization. For the indicated experiments, blebbistatin (Sigma) was added to the collagen/cell mixture at a final concentration of 20 μM prior to collagen polymerization.

Melanoma cells imaged near glass were embedded in an identical mixture of cells and collagen matrix polymerized in glass-bottom 96-well dishes (PerkinElmer). Confocal image stacks were acquired using a 60× (CFI Apo TIRF) objective on a Nikon Eclipse Ti microscope fitted with a Yokagawa spinning disk scan unit and Andor iXon emCCD camera.

Microscope Sample Preparation

The sample holder was prepared by heating 2% agarose with water, then solidifying this mixture in a custom mold (Figures 7B and 7C) to attach the agar sample holder to a stage-mounted dovetail. Once solidified, the sample holder was submerged in imaging medium before addition of the cell/collagen mixture. The imaging medium was either phenol red-free DMEM supplemented with 10% FBS or Leibovitz's L15 medium supplemented with 10% FBS for the melanoma or HBEC cells, respectively.

3D Image Rendering

All 3D volume renderings were performed using ImageJ (NIH), and all 3D surface renderings were performed using MATLAB (Mathworks). Image brightness and contrast were linearly adjusted prior to volume rendering. Since noise can obscure other features in 3D renderings, we median filtered the spheroid in Figure 2D, with a kernel radius of 1 pixel, and the cell in Figure 4B, with a kernel radius of 4 pixels. Segments of Movie S3, frames from which appear in Figures 4B and 4E, were also corrected for photobleaching by fitting the intensity of each cell over time to a decaying double exponential (Hodgson et al., 2006) and then normalizing the image intensity by the fit.

Optical Sectioning Characterization and Image Deconvolution

Optical sectioning in the axial direction for descanned and normal imaging modes was measured as described previously (Dean et al., 2015). Images were deconvolved as follows unless otherwise noted (Figure S6). The PSF was measured by ensemble averaging the 3D images of five individual 100 nm fluorescent nanospheres. We rotationally averaged the PSF about the axial direction to reduce noise. Using the averaged PSF we performed Wiener deconvolution (Sibarita, 2005). For cytoplasmically labeled cells, the Wiener parameter was estimated from each 3D frame following a rough segmentation of the cell. The signal was then measured as the average fluorescence intensity located within the cell and more than 5 pixels away from the cell boundary, and the noise was measured as the SD of the intensity located outside the cell and more than 20 pixels away from the cell boundary. Following the deconvolution, the images were apodized with an apodization filter that was defined by smoothing and then thresholding the optical transfer function (OTF) in the spatial frequency domain. The filter had a value of 1 at the origin and 0 at the boundary of the filter support volume determined by the OTF voxels above threshold. In between, the filter decayed linearly. The threshold value, which we term apodization height, was set by the user as a percentage (see below) of the maximum value of the OTF.

Characterization of Collagen Fibers

Collagen fibers were detected with 3D steerable curve filters (Aguet et al., 2005; González et al., 2009; Jacob and Unser, 2004). We performed multiscale detection by combining curve filters of widths 2–5 pixels. After filtering, the fiber skeletons were obtained by non-maximum suppression of the filter response. In Figure 3C the local fiber density was measured at every pixel as the percentage of fiber pixels retained after non-maximum suppression and thresholding that fell within a spherical volume of radius ~2 μm. This measure is readily interpretable as the local pixel occupancy of the thresholded non-maximum suppression image. The volume within the cell was excluded from the occupancy analysis and all pixels with local occupancies above 0.015 appear white. In Figure 3F, we measured the mean fiber density as a function of distance from the cell edge without locally smoothing the fiber density.

Fiber alignment toward the cell center was characterized by the nematic order parameter (Chaikin and Lubensky, 2000), which in three dimensions is

$$S = \langle P_2(\cos\theta)\rangle = \left\langle \frac{3\cos^2\theta - 1}{2} \right\rangle , \qquad \text{(Equation 1)}$$

where P_2 is the second order Legendre polynomial, and θ is the angle between the fiber alignment and the director, which we define here as the direction toward the cell center. Fibers aligned toward the cell center will have a nematic order parameter of 1, randomly aligned fibers will have an order parameter of 0, and those aligned in the plane perpendicular to the direction toward the cell center will have an order parameter of −1/2. Figure 3F shows the nematic order parameter as a function of distance from the cell edge, whereas for simplicity Figure 3E shows only $\cos\theta$, i.e., the dot product of the fiber alignment with the director. In Figure 3E, a value of 1 then indicates that the fiber is aligned toward the cell center and a value of 0 indicates that the fiber is perpendicular to the direction toward the cell center.

Cell Segmentation

Fluorescence movies of cytoplasmically labeled cells were deconvolved as described above. An apodization height of 0.05 was used for movies from which we measured bleb areas, whereas an apodization height of 0.07 was used for movies from which we tracked blebs since those movies were taken with a shorter exposure time. To preserve surface features, lower apodization heights were used for movies for which we calculated surface intensities. For each 3D image, we segmented cells by calculating first an Otsu threshold level, followed by a grayscale flood-fill operation, removal of small objects disconnected from the cell, and creation of an isosurface at the intensity level specified by the threshold (Figures 7D–7G) (Otsu, 1979). Mathematically, the isosurface is a triangulated mesh with each triangular face adjacent to one other face at each of its sides. We used MATLAB's isosurface function to generate the mesh from the processed image. Then we slightly smoothed the mesh geometry using curvature flow (Desbrun et al., 1999).

For images with multiple cells, we separately calculated an Otsu threshold level for each cell. The intensity histogram of an image with multiple cells tends to be composed of multiple signal peaks (the cells) and multiple background peaks, since the background intensity induced by the beam changes upon interacting with a cell. To threshold the foreground, we therefore calculated the corner intensity of the cumulative distribution function (CDF) of the pixel intensities. We defined the corner intensity as the intensity at which the CDF is closest to the coordinate corresponding to a pixel intensity of 0 and a cumulative probability of 1. This approach assumes that the large number of pixels in background intensity distributions are more narrowly banded in their intensity values than the more heterogeneous foreground intensity distributions. Using this corner value for a coarse foreground thresholding, we morphologically dilated each foreground connected component separately, and then calculated an Otsu threshold for each dilated region.

Bleb Detection and Tracking

Blebs are characterized by uniform or regular curvature. We measured the mean curvature at each triangular face as described in previous work (Figure S7G) (Elliott et al., 2015). Since curvature can be noisy, we median filtered surface curvature in 3D with a kernel radius of 1 pixel. We then further smoothed curvature by creating a graph of adjacent faces and smoothing curvature over the graph for 12 iterations,

$$S = \left(\frac{A}{3}\right)^k C , \qquad \text{(Equation 2)}$$

where S is the smoothed curvature, A is the adjacency matrix of the faces graph, k is the number of smoothing iterations, and C is the curvature.

To detect blebs, we performed a watershed segmentation of curvature over the graph of triangular faces (Figure 7H) (Mangan and Whitaker, 1999). The watershed algorithm oversegments blebs. We merged adjacent watershed regions in two different ways. First, in each frame we calculated the Otsu threshold level of smoothed mean curvature defined over the faces and labeled any watershed region that did not include a face with a curvature above the threshold as a flat region. For each non-flat region, we then calculated the spill depth (Mangan and Whitaker, 1999), defined as the largest curvature within the region minus the largest curvature at its boundary. The boundary of a region is composed of both the faces in the region that are adjacent to a non-flat region and the immediately adjacent faces in neighboring non-flat regions. We also defined the spill neighbor as the adjacent region with the largest curvature on the boundary. Starting with the greatest spill depth, we iteratively merged regions with their spill neighbors until no spill depth was greater than 0.6 times the Otsu curvature threshold.

We next merged adjacent regions by analyzing their configuration in 3D. For each region, including those labeled flat, we measured the closure surface area, σ, defined as the additional surface area needed to close the portion of the mesh occupied by the region. First we found the vertices at the edge of the region and calculated the mean position, v_m, of those vertices. Next, we closed the mesh by connecting the faces at the edge of the region to the vertex v_m. We next iteratively merged pairs of adjacent regions if the following condition was met,

$$\frac{\sigma_A + \sigma_B - \sigma_{AB}}{\sqrt{\sigma_A \sigma_B}} > \rho , \qquad \text{(Equation 3)}$$

where σ_A and σ_B are the closure surface areas of the two considered regions, σ_{AB} is the closure surface area of the two merged regions, and ρ is a parameter specified by the user. Here we used a ρ of 0.3. This condition is analogous to the law of cosines, and can be understood intuitively as merging pairs of regions that form a large angle relative to one another. A non-flat region was

allowed to merge with either a non-flat or flat region, but two flat regions were not allowed to merge.

To track blebs, we used the particle tracking software u-track (Jaqaman et al., 2008). Each bleb was modeled as a point particle with position and magnitude calculated as follows. The bleb position was defined as the mean position of the faces in the bleb with positive curvature, weighted by their curvature. The bleb magnitude was defined as the bleb surface area. In Figure 5, the tracked blebs are displayed in two different ways. In Figure 5H, faces at the bleb edge with negative curvature were iteratively removed from the bleb until all edge faces had non-negative curvature. In Figure 5F and Movie S4, the bleb locations are displayed as spheres at the location of the face that is the farthest from the iteratively shrunk bleb edge.

To assess the bleb segmentation workflow, we first visually inspected the cell segmentation by overlaying the extracted cell shape on each z plane of the original image (Figures S7A and S7B). We next examined bleb under-/oversegmentation. We created a graphical interface where users could rotate the cell surface and zoom in and out while selecting blebs by clicking. We compared the automated bleb segmentation (Figure S7C) with the blebs selected by five different users (Figure S7D). For the cell shown, the automated algorithm detected 105 blebs, whereas the users selected 91, 80, 80, 79, and 66 blebs. Of these 105 blebs, 60 were clicked on approximately once by each user, indicating that they were likely segmented correctly (Figures S7E and S7F), six were clicked on approximately twice and were likely undersegmented, and 28 were clicked on by one or no users and were likely oversegmented or otherwise not considered a bleb by the users. Since it is difficult even by eye to identify small blebs and distinguish merged blebs from a single frame alone, future work will likely need to incorporate temporal information. A gallery of bleb segmentations for seven different cells, with each frame chosen randomly, is shown for reference (Figure S7G).

Measuring Fluorescence Intensity on the Cell Surface

Following image deconvolution, we segmented the cell as described above, except that we did not smooth the mesh geometry. We next measured the intensity on the surface using the background-subtracted raw image. Each cell was depth normalized as described previously (Elliott et al., 2015). The intensity at each face on the mesh was defined as the mean intensity of the voxels inside the cell within a 1-μm radius of the face. The mean intensity on the surface of each cell was normalized to one.

The synthetic image of a blebby cell that is shown blurred in Figures 6A–6C consists of a large sphere with smaller spheres centered at its edge. The intensity inside this synthetic cell is 1, the intensity outside is 0, and the intensity at the edge is an intermediate value equal to the percentage of the voxel occupied by the synthetic cell body or blebs.

SUPPLEMENTAL INFORMATION

Supplemental Information includes seven figures, four movies, and one supplemental data zip file and can be found with this article online at http://dx.doi.org/10.1016/j.devcel.2016.01.022.

Example workflows with MATLAB code are provided in the meSPIM Supplemental Data zip file for describing and detecting collagen, segmenting blebs, and measuring intensity near the cell surface. To run the supplied code on the provided example, users will need to download the example data, meSPIM Example Dataset, from Mendeley Data at https://data.mendeley.com/ (http://dx.doi.org/10.17632/2dnn6n9w9w.1).

AUTHOR CONTRIBUTIONS

R.F., E.S.W., M.K.D., and G.D. conceived and designed the experiments. R.F. built the instrument. R.F., E.S.W., and K.M.D. performed experiments. C.S. prepared the HBEC cell spheroids. J.C. and M.Z.L. created the CyOFP protein. M.W.D. contributed reagents. M.K.D. and E.S.W. analyzed the data. M.K.D. wrote the analysis tools. R.F., E.S.W., M.K.D., K.M.D., C.S., and G.D. wrote the manuscript.

ACKNOWLEDGMENTS

We would like to thank John Hammer for the GFP-tractin construct, Magnus Höök for the CNA35 peptide, John Minna for the Kras^{V12} construct, Bob Fischer for the td-Tomato membrane marker construct, Wesley Burford and Kim Reed for molecular biology support, and Sean Morrison, Elena Piskounova, and Ugur Eskiocak for helping to establish the workflow for culturing primary melanoma. Some of the core functions and routines in the microscope control software are licensed under an MTA from Howard Hughes Medical Institute, Janelia Farm Research Campus. The full microscope control software code can be requested from the corresponding authors and will be distributed under MTAs with HHMI and UT Southwestern Medical Center. E.S.W., M.K.D., K.M.D., C.S., R.F., and G.D. were supported by Cancer Prevention Research Institute of Texas grant R1225 to G.D., and M.Z.L. and J.C. were supported by NIH grant 5DP1GM111003-02. M.K.D. was also supported by NIH grant F32-GM116370.

Received: April 9, 2015
Revised: November 11, 2015
Accepted: January 26, 2016
Published: February 22, 2016

REFERENCES

Aguet, F., Jacob, M., and Unser, M. (2005). Three-dimensional feature detection using optimal steerable filters. In Proceedings of the 2005 International Conference on Image Processing (ICIP), *Vol. 2*Proceedings of the 2005 International Conference on Image Processing (ICIP) (IEEE), pp. 1158–1161.

Ahrens, M.B., Orger, M.B., Robson, D.N., Li, J.M., and Keller, P.J. (2013). Whole-brain functional imaging at cellular resolution using light-sheet microscopy. Nat. Methods *10*, 413–420.

Baumgart, E., and Kubitscheck, U. (2012). Scanned light sheet microscopy with confocal slit detection. Opt. Express *20*, 21805–21814.

Blaser, H., Reichman-Fried, M., Castanon, I., Dumstrei, K., Marlow, F.L., Kawakami, K., Solnica-Krezel, L., Heisenberg, C.-P., and Raz, E. (2006). Migration of zebrafish primordial germ cells: a role for myosin contraction and cytoplasmic flow. Dev. Cell *11*, 613–627.

Brownfield, D.G., Venugopalan, G., Lo, A., Mori, H., Tanner, K., Fletcher, D.A., and Bissell, M.J. (2013). Patterned collagen fibers orient branching mammary epithelium through distinct signaling modules. Curr. Biol. *23*, 703–709.

Chaikin, P.M., and Lubensky, T.C. (2000). Principles of Condensed Matter Physics (Cambridge University Press).

Charras, G.T. (2008). A short history of blebbing. J. Microsc. *231*, 466–478.

Charras, G., and Paluch, E. (2008). Blebs lead the way: how to migrate without lamellipodia. Nat. Rev. Mol. Cell Biol. *9*, 730–736.

Charras, G.T., Yarrow, J.C., Horton, M.A., Mahadevan, L., and Mitchison, T.J. (2005). Non-equilibration of hydrostatic pressure in blebbing cells. Nature *435*, 365–369.

Charras, G.T., Hu, C.-K., Coughlin, M., and Mitchison, T.J. (2006). Reassembly of contractile actin cortex in cell blebs. J. Cell Biol. *175*, 477–490.

Charras, G.T., Coughlin, M., Mitchison, T.J., and Mahadevan, L. (2008). Life and times of a cellular bleb. Biophys. J. *94*, 1836–1853.

Chen, B.-C., Legant, W.R., Wang, K., Shao, L., Milkie, D.E., Davidson, M.W., Janetopoulos, C., Wu, X.S., Hammer, J.A., Liu, Z., et al. (2014). Lattice light-sheet microscopy: imaging molecules to embryos at high spatiotemporal resolution. Science *346*, 1257998.

Conklin, M.W., Eickhoff, J.C., Riching, K.M., Pehlke, C.A., Eliceiri, K.W., Provenzano, P.P., Friedl, A., and Keely, P.J. (2011). Aligned collagen is a prognostic signature for survival in human breast carcinoma. Am. J. Pathol. *178*, 1221–1232.

Dean, K.M., and Fiolka, R. (2014). Uniform and scalable light-sheets generated by extended focusing. Opt. Express *22*, 26141–26152.

Dean, K.M., Roudot, P., Welf, E.S., Danuser, G., and Fiolka, R. (2015). Deconvolution-free subcellular imaging with axially swept light sheet microscopy. Biophys. J. *108*, 2807–2815.

Desbrun, M., Meyer, M., Schröder, P., and Barr, A.H. (1999). Implicit fairing of irregular meshes using diffusion and curvature flow. In Proceedings of the 26th Annual Conference on Computer Graphics and Interactive Techniques (ACM Press/Addison-Wesley), pp. 317–324.

Dinic, J., Ashrafzadeh, P., and Parmryd, I. (2013). Actin filaments attachment at the plasma membrane in live cells cause the formation of ordered lipid domains. Biochim. Biophys. Acta *1828*, 1102–1111.

Discher, D.E., Mooney, D.J., and Zandstra, P.W. (2009). Growth factors, matrices, and forces combine and control stem cells. Science *324*, 1673–1677.

Diz-Muñoz, A., Krieg, M., Bergert, M., Ibarlucea-Benitez, I., Muller, D.J., Paluch, E., and Heisenberg, C.-P. (2010). Control of directed cell migration in vivo by membrane-to-cortex attachment. PLoS Biol. *8*, e1000544.

Driscoll, M.K., and Danuser, G. (2015). Quantifying modes of 3D cell migration. Trends Cell Biol. *25*, 749–759.

Elliott, H., Fischer, R.S., Myers, K.A., Desai, R.A., Gao, L., Chen, C.S., Adelstein, R.S., Waterman, C.M., and Danuser, G. (2015). Myosin II controls cellular branching morphogenesis and migration in three dimensions by minimizing cell-surface curvature. Nat. Cell Biol. *17*, 137–147.

Fackler, O.T., and Grosse, R. (2008). Cell motility through plasma membrane blebbing. J. Cell Biol. *181*, 879–884.

Fahrbach, F.O., and Rohrbach, A. (2012). Propagation stability of self-reconstructing Bessel beams enables contrast-enhanced imaging in thick media. Nat. Commun. *3*, 632.

Fahrbach, F.O., Simon, P., and Rohrbach, A. (2010). Microscopy with self-reconstructing beams. Nat. Photon. *4*, 780–785.

Fiolka, R., Stemmer, A., and Belyaev, Y. (2007). Virtual slit scanning microscopy. Histochem. Cell Biol. *128*, 499–505.

Gao, L., Shao, L., Higgins, C.D., Poulton, J.S., Peifer, M., Davidson, M.W., Wu, X., Goldstein, B., and Betzig, E. (2012). Noninvasive imaging beyond the diffraction limit of 3D dynamics in thickly fluorescent specimens. Cell *151*, 1370–1385.

Girton, T.S., Oegema, T.R., Grassl, E.D., Isenberg, B.C., and Tranquillo, R.T. (2000). Mechanisms of stiffening and strengthening in media-equivalents fabricated using glycation. J. Biomech. Eng. *122*, 216–223.

Gligorijevic, B., Bergman, A., and Condeelis, J. (2014). Multiparametric classification links tumor microenvironments with tumor cell phenotype. PLoS Biol. *12*, e1001995.

González, G., Aguet, F., Fleuret, F., Unser, M., and Fua, P. (2009). Steerable features for statistical 3D dendrite detection. Med. Image Comput. Comput. Assist. Interv. *12*, 625–632.

Goswami, D., Gowrishankar, K., Bilgrami, S., Ghosh, S., Raghupathy, R., Chadda, R., Vishwakarma, R., Rao, M., and Mayor, S. (2008). Nanoclusters of GPI-anchored proteins are formed by cortical actin-driven activity. Cell *135*, 1085–1097.

Harding, A.S., and Hancock, J.F. (2008). Using plasma membrane nanoclusters to build better signaling circuits. Trends Cell Biol. *18*, 364–371.

Haugh, J.M., Codazzi, F., Teruel, M., and Meyer, T. (2000). Spatial sensing in fibroblasts mediated by 3′ phosphoinositides. J. Cell Biol. *151*, 1269–1280.

Hirata, E., Girotti, M.R., Viros, A., Hooper, S., Spencer-Dene, B., Matsuda, M., Larkin, J., Marais, R., and Sahai, E. (2015). Intravital imaging reveals how BRAF inhibition generates drug-tolerant microenvironments with high integrin β1/FAK signaling. Cancer Cell *27*, 574–588.

Hodgson, L., Nalbant, P., Shen, F., and Hahn, K. (2006). Imaging and photobleach correction of Mero-CBD, sensor of endogenous Cdc42 activation. Methods Enzymol. *406*, 140–156.

Huisken, J., and Stainier, D.Y.R. (2009). Selective plane illumination microscopy techniques in developmental biology. Development *136*, 1963–1975.

Huisken, J., Swoger, J., Del Bene, F., Wittbrodt, J., and Stelzer, E.H.K. (2004). Optical sectioning deep inside live embryos by selective plane illumination microscopy. Science *305*, 1007–1009.

Jacob, M., and Unser, M. (2004). Design of steerable filters for feature detection using canny-like criteria. IEEE Trans. Pattern Anal. Mach. Intell. *26*, 1007–1019.

Jaqaman, K., Loerke, D., Mettlen, M., Kuwata, H., Grinstein, S., Schmid, S.L., and Danuser, G. (2008). Robust single-particle tracking in live-cell time-lapse sequences. Nat. Methods *5*, 695–702.

Johnson, H.W., and Schell, M.J. (2009). Neuronal IP3 3-kinase is an F-actin-bundling protein: role in dendritic targeting and regulation of spine morphology. Mol. Biol. Cell *20*, 5166–5180.

Kanchanawong, P., Shtengel, G., Pasapera, A.M., Ramko, E.B., Davidson, M.W., Hess, H.F., and Waterman, C.M. (2010). Nanoscale architecture of integrin-based cell adhesions. Nature *468*, 580–584.

Kapustina, M., Elston, T.C., and Jacobson, K. (2013). Compression and dilation of the membrane-cortex layer generates rapid changes in cell shape. J. Cell Biol. *200*, 95–108.

Keller, P.J. (2013). Imaging morphogenesis: technological advances and biological insights. Science *340*, 1234168.

Keller, P.J., Schmidt, A.D., Wittbrodt, J., and Stelzer, E.H.K. (2008). Reconstruction of Zebrafish early embryonic development by scanned light sheet microscopy. Science *322*, 1065–1069.

Keller, P.J., Schmidt, A.D., Santella, A., Khairy, K., Bao, Z., Wittbrodt, J., and Stelzer, E.H.K. (2010). Fast, high-contrast imaging of animal development with scanned light sheet-based structured-illumination microscopy. Nat. Methods *7*, 637–642.

Laser-Azogui, A., Diamant-Levi, T., Israeli, S., Roytman, Y., and Tsarfaty, I. (2013). Met-induced membrane blebbing leads to amoeboid cell motility and invasion. Oncogene *33*, 1788–1798.

Lee, K., Elliott, H.L., Oak, Y., Zee, C.-T., Groisman, A., Tytell, J.D., and Danuser, G. (2015). Functional hierarchy of redundant actin assembly factors revealed by fine-grained registration of intrinsic image fluctuations. Cell Syst. *1*, 37–50.

Liu, Y.-J., Le Berre, M., Lautenschlaeger, F., Maiuri, P., Callan-Jones, A., Heuzé, M., Takaki, T., Voituriez, R., and Piel, M. (2015). Confinement and low adhesion induce fast amoeboid migration of slow mesenchymal cells. Cell *160*, 659–672.

Ma, X., Schickel, M.E., Stevenson, M.D., Sarang-Sieminski, A.L., Gooch, K.J., Ghadiali, S.N., and Hart, R.T. (2013). Fibers in the extracellular matrix enable long-range stress transmission between cells. Biophys. J. *104*, 1410–1418.

Mangan, A.P., and Whitaker, R.T. (1999). Partitioning 3D surface meshes using watershed segmentation. IEEE Trans. Vis. Comput. Graph. *5*, 308–321.

Melvin, A.T., Welf, E.S., Wang, Y., Irvine, D.J., and Haugh, J.M. (2011). In chemotaxing fibroblasts, both high-fidelity and weakly biased cell movements track the localization of PI3K signaling. Biophys. J. *100*, 1893–1901.

Otsu, N. (1979). A threshold selection method from gray-level histograms. IEEE Trans. Syst. Man Cybern. *9*, 62–66.

Paluch, E.K., and Raz, E. (2013). The role and regulation of blebs in cell migration. Curr. Opin. Cell Biol. *25*, 582–590.

Pampaloni, F., Reynaud, E.G., and Stelzer, E.H.K. (2007). The third dimension bridges the gap between cell culture and live tissue. Nat. Rev. Mol. Cell Biol. *8*, 839–845.

Pawley, J. (2010). Handbook of Biological Confocal Microscopy (Springer Science & Business Media).

Pickup, M.W., Mouw, J.K., and Weaver, V.M. (2014). The extracellular matrix modulates the hallmarks of cancer. EMBO Rep. *15*, 1243–1253.

Planchon, T.A., Gao, L., Milkie, D.E., Davidson, M.W., Galbraith, J.A., Galbraith, C.G., and Betzig, E. (2011). Rapid three-dimensional isotropic imaging of living cells using Bessel beam plane illumination. Nat. Methods *8*, 417–423.

Plotnikov, S.V., Pasapera, A.M., Sabass, B., and Waterman, C.M. (2012). Force fluctuations within focal adhesions mediate ECM-rigidity sensing to guide directed cell migration. Cell *151*, 1513–1527.

Provenzano, P.P., Eliceiri, K.W., Campbell, J.M., Inman, D.R., White, J.G., and Keely, P.J. (2006). Collagen reorganization at the tumor-stromal interface facilitates local invasion. BMC Med. *4*, 38.

Provenzano, P.P., Inman, D.R., Eliceiri, K.W., and Keely, P.J. (2009). Matrix density-induced mechanoregulation of breast cell phenotype, signaling and gene expression through a FAK–ERK linkage. Oncogene *28*, 4326–4343.

Rao, S.S., Bentil, S., DeJesus, J., Larison, J., Hissong, A., Dupaix, R., Sarkar, A., and Winter, J.O. (2012). Inherent interfacial mechanical gradients in 3D hydrogels influence tumor cell behaviors. PLoS One *7*, e35852.

Reynaud, E.G., Peychl, J., Huisken, J., and Tomancak, P. (2015). Guide to light-sheet microscopy for adventurous biologists. Nat. Methods *12*, 30–34.

Roy, R., Boskey, A., and Bonassar, L.J. (2010). Processing of type I collagen gels using nonenzymatic glycation. J. Biomed. Mater. Res. A *93*, 843–851.

Rubashkin, M.G., Cassereau, L., Bainer, R., DuFort, C.C., Yui, Y., Ou, G., Paszek, M.J., Davidson, M.W., Chen, Y.-Y., and Weaver, V.M. (2014). Force engages vinculin and promotes tumor progression by enhancing PI3K activation of phosphatidylinositol (3,4,5)-triphosphate. Cancer Res. *74*, 4597–4611.

Ruprecht, V., Wieser, S., Callan-Jones, A., Smutny, M., Morita, H., Sako, K., Barone, V., Ritsch-Marte, M., Sixt, M., Voituriez, R., et al. (2015). Cortical contractility triggers a stochastic switch to fast amoeboid cell motility. Cell *160*, 673–685.

Sato, M., Larsen, J.E., Lee, W., Sun, H., Shames, D.S., Dalvi, M.P., Ramirez, R.D., Tang, H., DiMaio, J.M., Gao, B., et al. (2013). Human lung epithelial cells progressed to malignancy through specific oncogenic manipulations. Mol. Cancer Res. *11*, 638–650.

Shi, Q., Ghosh, R.P., Engelke, H., Rycroft, C.H., Cassereau, L., Sethian, J.A., Weaver, V.M., and Liphardt, J.T. (2014). Rapid disorganization of mechanically interacting systems of mammary acini. Proc. Natl. Acad. Sci. USA *111*, 658–663.

Sibarita, J.-B. (2005). Deconvolution microscopy. In Microscopy Techniques, J. Rietdorf, ed. (Springer), pp. 201–243.

Spiller, D.G., Wood, C.D., Rand, D.A., and White, M.R.H. (2010). Measurement of single-cell dynamics. Nature *465*, 736–745.

Stelzer, E.H.K. (2015). Light-sheet fluorescence microscopy for quantitative biology. Nat. Methods *12*, 23–26.

Swoger, J., Verveer, P., Greger, K., Huisken, J., and Stelzer, E.H.K. (2007). Multi-view image fusion improves resolution in three-dimensional microscopy. Opt. Express *15*, 8029–8042.

Teruel, M.N., and Meyer, T. (2000). Translocation and reversible localization of signaling proteins: a dynamic future for signal transduction. Cell *103*, 181–184.

Thievessen, I., Fakhri, N., Steinwachs, J., Kraus, V., McIsaac, R.S., Gao, L., Chen, B.-C., Baird, M.A., Davidson, M.W., Betzig, E., et al. (2015). Vinculin is required for cell polarization, migration, and extracellular matrix remodeling in 3D collagen. FASEB J. *29*, 4555–4567.

Verveer, P.J., Swoger, J., Pampaloni, F., Greger, K., Marcello, M., and Stelzer, E.H.K. (2007). High-resolution three-dimensional imaging of large specimens with light sheet-based microscopy. Nat. Methods *4*, 311–313.

Vettenburg, T., Dalgarno, H.I.C., Nylk, J., Coll-Lladó, C., Ferrier, D.E.K., Čižmár, T., Gunn-Moore, F.J., and Dholakia, K. (2014). Light-sheet microscopy using an Airy beam. Nat. Methods *11*, 541–544.

Vilela, M., Halidi, N., Besson, S., Elliott, H., Hahn, K., Tytell, J., and Danuser, G. (2013). Fluctuation analysis of activity biosensor images for the study of information flow in signaling pathways. Methods Enzymol. *519*, 253–276.

Wang, E., Babbey, C.M., and Dunn, K.W. (2005). Performance comparison between the high-speed Yokogawa spinning disc confocal system and single-point scanning confocal systems. J. Microsc. *218*, 148–159.

Wang, H., Abhilash, A.S., Chen, C., Wells, R., and Shenoy, V. (2014). Long-range force transmission in fibrous matrices enabled by tension-driven alignment of fibers. Biophys. J. *107*, 2592–2603.

Weiger, M.C., Ahmed, S., Welf, E.S., and Haugh, J.M. (2010). Directional persistence of cell migration coincides with stability of asymmetric intracellular signaling. Biophys. J. *98*, 67–75.

Welf, E.S., and Danuser, G. (2014). Using fluctuation analysis to establish causal relations between cellular events without experimental perturbation. Biophys. J. *107*, 2492–2498.

Welf, E.S., Ahmed, S., Johnson, H.E., Melvin, A.T., and Haugh, J.M. (2012). Migrating fibroblasts reorient directionality by a metastable, PI3K-dependent mechanism. J. Cell Biol. *197*, 105–114.

Wilson, T. (1995). The role of the pinhole in confocal imaging system. In Handbook of Biological Confocal Microscopy, J.B. Pawley, ed. (Springer), pp. 167–182.

Xu, Y., Rivas, J.M., Brown, E.L., Liang, X., and Höök, M. (2004). Virulence potential of the staphylococcal adhesin CNA in experimental arthritis is determined by its affinity for collagen. J. Infect. Dis. *189*, 2323–2333.

Yi, J., Wu, X.S., Crites, T., and Hammer, J.A. (2012). Actin retrograde flow and actomyosin II arc contraction drive receptor cluster dynamics at the immunological synapse in Jurkat T cells. Mol. Biol. Cell *23*, 834–852.